Enhanced electric field sensitivity of quantum dot/rod two-photon fluorescence and its relevance for cell transmembrane voltage imaging

Stijn Jooken, Yovan de Coene, Olivier Deschaume, Dániel Zámbó, Tangi Aubert, Zeger Hens, Dirk Dorfs, Thierry Verbiest, Koen Clays, Geert Callewaert, et al.

Research article

Stijn Jooken*, Yovan de Coene, Olivier Deschaume, Dániel Zámbó, Tangi Aubert, Zeger Hens, Dirk Dorfs, Thierry Verbiest, Koen Clays, Geert Callewaert and Carmen Bartic*

Enhanced electric field sensitivity of quantum dot/rod two-photon fluorescence and its relevance for cell transmembrane voltage imaging

https://doi.org/10.1515/nanoph-2021-0077
Received February 23, 2021; accepted May 4, 2021; published online May 21, 2021

Abstract: The optoelectronic properties of semiconductor nanoparticles make them valuable candidates for the long-term monitoring of transmembrane electric fields in excitable cells. In this work, we show that the electric field sensitivity of the fluorescence intensity of type-I and quasi-type-II quantum dots and quantum rods is enhanced under two-photon excitation compared to single-photon excitation. Based on the superior electric field sensitivity of the two-photon excited fluorescence, we demonstrate the ability of quantum dots and rods to track fast switching E-fields. These findings indicate the potential of semiconductor nanoparticles as cellular voltage probes in multiphoton imaging.

***Corresponding authors: Stijn Jooken and Carmen Bartic**, Department of Physics and Astronomy, Soft Matter and Biophysics, KU Leuven, 3001 Leuven, Belgium, E-mail: stijn.jooken@kuleuven.be (S. Jooken), carmen.bartic@kuleuven.be (C. Bartic). https://orcid.org/0000-0003-4787-9086 (S. Jooken). https://orcid.org/0000-0001-9577-2844 (C. Bartic)
Yovan de Coene, Thierry Verbiest and Koen Clays, Department of Chemistry, Molecular Imaging and Photonics, KU Leuven, 3001 Leuven, Belgium. https://orcid.org/0000-0002-1514-5865 (Y. de Coene). https://orcid.org/0000-0002-0822-176X (T. Verbiest). https://orcid.org/0000-0001-9490-0023 (K. Clays)
Olivier Deschaume, Department of Physics and Astronomy, Soft Matter and Biophysics, KU Leuven, 3001 Leuven, Belgium. https://orcid.org/0000-0001-6222-0947
Dániel Zámbó and Dirk Dorfs, Institute of Physical Chemistry and Electrochemistry, Leibniz Universität Hannover, 30167 Hannover, Germany. https://orcid.org/0000-0001-7671-039X (D. Zámbó). https://orcid.org/0000-0001-6175-4891 (D. Dorfs)
Tangi Aubert, Department of Chemistry, Ghent University, 9000 Ghent, Belgium; and ICGM, University of Montpellier, CNRS, ENSCM, 34000 Montpellier, France. https://orcid.org/0000-0003-0905-3822
Zeger Hens, Department of Chemistry, Ghent University, 9000 Ghent, Belgium. http://orcid.org/0000-0002-7041-3375
Geert Callewaert, Department of Cellular and Molecular Medicine, KU Leuven Campus Kulak, 8500 Kortrijk, Belgium

Keywords: electric field; quantum dot/rod; semiconductor nanoparticle; two-photon fluorescence; voltage sensing.

1 Introduction

Quantum dots (QDs) or quantum rods (QRs) are semiconductor nanoparticles (NP) typically composed of II–VI, III–V or IV–VI materials such as CdSe, CdS, InP or PbS among others. Their sizes are smaller than the Bohr exciton radius giving them unique optical and optoelectronic properties due to the confinement of the charge carriers in all three dimensions. As a consequence, quantum dots have a broad absorbance and a narrow emission spectrum (ideal for fluorescence multiplexing) that can be tuned by simply varying the size of the particle. Their quantum yields (QY) and long-term photostability are much less affected by photobleaching than those of organic fluorophores. Moreover, the much larger absorption cross-sections for both single- and two-photon excited fluorescence (1PF & 2PF), even up to 10^6–10^7 GM [1, 2], justify why QDs are extensively used in biological imaging applications [3, 4].

To reduce the probability of nonradiative decay through surface states and guarantee a high fluorescence QY, the most commonly used QDs are semiconductor core–shell heterostructures, in which a second material with a different band alignment is epitaxially grown around the semiconductor core. In a type-I structure, the bandgap of the core material is smaller than the bandgap of the shell. In these structures, the shell effectively passivates the surface of the core, reducing the number of surface dangling bonds, enhancing the fluorescence QY and photochemical stability. In a type-II or quasi-type-II structure, either the conduction or valence band of the core material is located within the bandgap of the shell in a staggered fashion. As a consequence, one carrier is confined to the core while the other is either located in the shell or delocalized over the entire particle. The latter is referred to as a quasi-type-II NP.

Because of their 3D confinement, a QD's fluorescence can be modulated by external electrical fields through a combination of the Quantum-confined Stark effect (QCSE) and QD ionization [5]. In the QCSE, an external electric field separates the charge carriers, creating a dipole moment. Consequently, the reduced overlap between the electron and hole wave functions enhances the nonradiative decay resulting in a decrease of the fluorescence intensity. In a symmetric QD, the decrease of the fluorescence emission intensity due to the QCSE is known to be quadratic with the applied E-field [6]. In an asymmetric QR, on the other hand, consisting of a QD core overgrown with a rod-shaped shell, the QCSE results in a linear decrease of the fluorescence intensity [7, 8]. Carrier ionization entails the possibility that upon photoexcitation a core carrier, electron or hole, is thermally ejected or tunnels to the QD's surface. Any surface defect can potentially act as a trap state and capture the ejected charge carrier. Photoexcitation of such an ionized QD then triggers nonradiative Auger recombination, which also quenches the fluorescence. In the presence of an external electric field, the confinement barrier is reduced, increasing the population of nonfluorescing, ionized QDs, also decreasing the fluorescence intensity [9].

In the last decade, several studies have investigated the electric field sensitivity of the fluorescence intensity [5, 8, 10, 11], the spectral shift of the emission wavelength [7, 10, 12–14] and the radiative lifetime [7] of different types of semiconductor heterostructures under single-photon (1P) illumination in a controlled environment. While lifetime and spectral imaging are promising detection schemes as well, standard fluorescence intensity microscopy is the most wide spread imaging modality in microscopy and electrophysiology labs and hence the focus of this work. Table 1 gives an overview of the reported voltage sensitivities of the fluorescence intensity to applied E-fields of different types of QDs (omitting reported spectral shifts and lifetime imaging). It clearly shows that type-II and quasi-type-II NPs exhibit much larger sensitivities compared to type-I NPs. However, previous reports only studied 1PF changes and mostly investigated the E-field sensitivity of dry or polymer encapsulated NPs.

As such, the use of QDs has progressed in imaging cellular membrane potentials, competing with voltage-sensitive dyes and genetically encoded voltage indicators (GEVIs) or hybrids thereof [15], which still suffer from low brightness, photobleaching, toxicity and/or need for genetic manipulation. In principle, semiconductor NPs offer a robust alternative capable of overcoming such limitations.

To circumvent problems with QD membrane insertion, initial reports opted for an indirect modulation of fluorescence through electron transfer [16] or Förster resonance energy transfer [17]. Recently lipid-coated type-II QRs have been embedded within the cell membrane to successfully report

Table 1: Literature reports on QCSE-based E-field sensitivity of QD/QR 1PF intensity by application of well-controlled E-fields.

Nanoparticle	Ø (nm)	Capping	Applied E-field	$\Delta F/F_0$	Ref.
Quasi-type-II CdSe/CdS QD	5	Bipyridine In aqueous, ionic solution	Steady-state, 1 Hz, 20 Hz Ensemble	0% below 250 kV/cm 60% for 900 kV/cm	[8]
Type-I InP/ZnS QD	5			0% below 250 kV/cm 70% for 900 kV/cm	
Type-I CdSe/ZnS QD	6	TOPO[a], oleic acid, oleylamine,	8 Hz	0 ± 7% for 400 kV/cm	[11]
Quasi-type-II CdS/CdSe/CdS	12	hexadecylamine Embedded in a PVP[b] layer	Single particle	−40 ± 20% and 50 ± 35% for 400 kV/cm	
Quasi-type-II Te-doped CdSe/CdS QR	40			−33 ± 7% and 38 ± 14% for 400 kV/cm	
Quasi-type-II CdSe/CdS QR	40			11 ± 12% for 400 kV/cm	
Type-II ZnSe/CdS QR	7 × 12			−42 ± 16% and 69 ± 32% for 400 kV/cm	
Type-I CdSe/ZnS QD	5.3	Oleylamine, oleic acid, TOPO Embedded in PMMA film	Steady-state Ensemble	2% for 100 kV/cm 22% for 500 kV/cm	[5]
Quasi-type-II CdSe/ZnSe QD	7			5% for 100 kV/cm 63% for 500 kV/cm	
CdSe QR	43 × 4	TOPO, oleic acid,	10 Hz	16.4% for 400 kV/cm	[10]
Quasi-type-II CdSe/CdS QRs	29 × 4	octadecylamine, oleylamine	Single particle	30.2% for 400 kV/cm	
Type-II CdTe/CdSe QDs	6	Air exposed		<15% for 400 kV/cm	
Asymmetric hammer-shaped Type-II CdSe/CdS/CdZnSe	28 × 5 × 3			36.5% for 400 kV/cm	

[a]Trioctylphosphine oxide, [b]polyvinylpyrrolidone.

patch-clamp induced changes in membrane potential in HEK293 cells [18, 19] and mouse cortical neurons [20]. However, Ludwig et al. [20] reported limited (less than 10%) success in membrane insertion with varying degree of insertion and orientation (ideally orthogonal). Even with extensive image processing, only few responsive NPs (0.6% of 1242 analyzed particles in 35 cells) were found. At a single particle level, QR fluorescence exhibited short intervals of voltage sensitivity with a mean $\Delta F/F_0$ of 5–10% (0.6 nm wavelength shift) for a 25 Hz voltage square wave with 60 mV amplitude (~150 kV/cm), which is only slightly smaller to the expected response in calibration experiments on particles with a similar shape and composition [11].

Remarkably, two-photon (2P) imaging of direct modulation of a QDs fluorescence by external electric fields is an unexplored territory. While the nonlinear optical properties of semiconductor NPs are a main area of interest in photonic material research, especially their 2P absorption (2PA) cross-sections, so far only the effect of temperature changes on the 2PF was investigated [21]. The thermal sensitivity was found to be enhanced with respect to 1P excitation and attributed to a temperature sensitive 2PA cross-section. In general, multi-photon bio-imaging benefits from a reduced photobleaching and better spatial resolution due to a reduced excitation volume as well as an increased penetration depth, reduced tissue damage and autofluorescence at near-infrared (NIR) excitation wavelengths. We have previously used 2P imaging to report fluorescence changes occurring during the electrical and contractile activity of spontaneously beating cardiomyocytes [22].

In an effort to further elucidate the potential of QDs for imaging membrane voltages in electrogenic cells, we report here the electric field sensitivity of 1PF and 2PF of colloidal QDs and QRs upon transfer to the water phase. We show for the first time that under 2P excitation, the electric field sensitivity is enhanced with respect to 1P excitation for three different water-solubilized NPs, a type-I CdSe/ZnS QD with a 3.9 nm core size and a 6.3 nm total diameter, a quasi-type-II CdSe/CdS QD with a 3.7 nm core size and 8.9 nm total diameter and a quasi-type-II CdSe/CdS dot-in-rod with a 3.7 nm core size, 35 nm length and 5 nm width. These particles are henceforth referred to as QD6, QD9 and QR35, respectively. All three NPs have narrow emission spectra with respective center wavelengths 630, 640 and 610 nm. Using microfabricated gold interdigitated electrodes (IDE) [12, 22] we applied electric fields up to 600 kV/cm and report both steady-state fluorescence changes and the fluorescence modulation in AC (alternating current) fields of 0–250 kV/cm with frequencies ranging from 0.5 to 10 Hz. Based on the analysis of the 1PF and 2PF responses to transient electric fields, we conclude that the optoelectronic characteristics of our best performing NPs make them suitable for detecting cardiac APs by 2P imaging with an E-field sensitivity ($\Delta F/F_0$) of roughly 14% compared to a 1PF sensitivity of 8%.

2 Materials and methods

2.1 Materials

Cadmium oxide (CdO, 99.998%), oleic acid (OA, 90%) were purchased from Alfa Aesar. Tri-*n*-octylphosphine oxide (TOPO, 99%), elemental sulfur (99.98%), 1-octadecene (ODE, 90%), poly-styrene-*co*-maleic anhydride (PSMA, 1700 g/mol), mercaptosuccinic acid (MSA), Jeffamine polyetheramine (M600), ethanolamine ($ethNH_2$), chloroform (≥$CHCl_3$, 99.8%), tetramethylammonium hydroxide pentahydrate (TMAH, ≥95.0%), 4-(2-hydroxyethyl)-1-piperazineethanesulfonic acid (HEPES) and collagen from bovine skin (6 mg/mL) were purchased from Sigma-Aldrich. Toluene (≥99.7%) and methanol (MeOH, ≥99.8%), sulfuric acid (H_2SO_4), hydrogen peroxide (H_2O_2, 31%) were purchased from Honeywell. Hexamethyldisilazane (HMDS), 1-methyl-2-pyrrolidone (NMP) and Microposit S1818 G2 were purchased from Microchemicals. Tri-*n*-octylphosphine (TOP, 97%), octadecylphosphonic acid (ODPA, 99.0%) and hexylphosphonic acid (HPA, 99%) were obtained from Fisher Scientific and PCI, respectively. All chemicals were used as received without further purification.

2.2 NP synthesis and water-transfer

The 6 nm octadecylamine capped type-I CdSe/ZnS QDs (QD6) were purchased from Sigma-Aldrich (product n° 790206). The 9 nm oleic acid capped quasi-type-II CdSe/CdS QDs (QD9) were synthesized according to the *flash* procedure [23, 24]. CdO (0.183 g), TOPO (5 g) and OA (2.5 g) were degassed in a Schlenk-line system at 150 °C for 1 h. After changing the vacuum to nitrogen, the temperature was set to 350 °C. After the complete dissolution of the CdO, TOP (1 mL) was injected. After the temperature had recovered to 350 °C, a solution of CdSe QDs (0.2 µmol) mixed with TOP:S (600 µL containing 40 mg elemental sulfur) and TOP (1.4 mL) was rapidly injected. After 5 min reaction time, the solution was cooled down to 80 °C, at which point toluene (1 mL) was injected. At 40 °C, the solution was precipitated via the addition of MeOH (3 mL) and centrifuged. The QDs were further purified twice using toluene and MeOH as solvent and nonsolvent, respectively. Finally, the QDs were redispersed in toluene. The dot (3.5 nm) in rod (5 × 35 nm) phosphonic acid capped quasi-type-II CdSe/CdS QRs (QR35) were synthesized according to Carbone et al. [25] with slight modifications. CdO (0.36 g), HPA (0.48 g), ODPA (1.74 g) and TOPO (18.0 g) were degassed in a Schlenk-line system at 150 °C for 45 min under stirring. After changing from vacuum to argon, the temperature was set to 300 °C. After the complete dissolution of the CdO (20–40 min), TOP (10.8 mL) was injected swiftly. Ten minutes later, the temperature was raised to 350 °C and the toluene solution of the CdSe QDs (0.48 µmol) mixed with TOP:S solution (16.62 mL containing 1.20 g elemental sulfur) was rapidly injected with a glass syringe. After 8 min reaction time, the solution was cooled down to 80 °C, at which point toluene (10 mL) was injected. At 40 °C, the solution was precipitated via the addition of MeOH (10 mL) and centrifuged (3750 g, 10 min). The dot-in-rods were centrifuged and redispersed in toluene in three consecutive cycles. Finally, the

particles were redispersed in 6 mL toluene (final Cd concentration: ca. 70 g/L). Transmission electron microscopy (TEM) images of the particles can be found in SI (Figure S1).

The NPs were first transferred from their initial organic solvent to water. All types of NPs were transferred by encapsulation of their respective native ligands with PSMA using a slightly modified protocol with respect to that described by Lees et al. [26]. Half of the anhydride rings were opened with a Jeffamine M-600 polyetheramine, which consists of nine polypropylene glycol (PPG) units and one polyethylene glycol (PEG) unit, and the remainder was opened using ethNH$_2$. The presence of the M600 provided steric stabilization in addition to the electrostatic repulsion provided by the carboxylate residues from the opened maleic anhydride rings. In the optimized protocols, 47 mg PSMA was dissolved in 50 µL chloroform ($CHCl_3$) and added to 50 µL of the 1 µM QR35 stock solution, 30 mg PSMA was combined with 100 µL of a 10 µM QD6 stock solution and 15 mg PSMA with 100 µL of 1 µM QD9 stock solution. After 4 h of shaking, 47, 30 and 15 µL of M600 was added, respectively, followed by 100 µL of ethNH$_2$ in 500 µL of water 3 h later. After vigorous shaking for 10 min, the $CHCl_3$ was evaporated using a rotary evaporator at 250 mbar, 40 °C. The resulting NP suspension was centrifuged and passed through a PD10 desalting column (GE Healthcare) to remove excess ligands. Alternatively to the PSMA encapsulation, some of the type-I CdSe/ZnS QDs (6 nm) were also transferred by ligand exchange with MSA by combining 20 mg MSA with 100 µL of a 10 µM QD6 stock solution in the presence of an equal volume of water and buffered at pH 10 using TMAH [27, 28]. And some of the quasi-type-II CdSe/CdS QDs (9 nm) were transferred by coating with an 8.5 nm thick silica shell via the reverse microemulsion method as described by Aubert et al. [29] (see SI for details). This method likely involves an exchange of the native ligands [30]. These silica-coated CdSe/CdS NPs were further functionalized with PEG ligands (9–12 PE units) to enhance colloidal stability and prevent particle aggregation [31]. All water-transferred NPs were purified and stored in a 20 mM pH 7.4 aqueous HEPES buffer at a concentration of 200 nM. Only the QD6-MSA was stored at pH 10 in an excess of MSA to prevent rapid degradation of the organic coating. Absorbance and emission spectra after water-transfer can be found in SI (Figure S2).

2.3 QY yield

The QY of the NPs were determined in 20 mM pH 7.4 HEPES buffer relative to rhodamine 6G (reference QY of 0.96 [32]) according to the method described by Würth et al. [33]. Absorbance was measured using a GE Healthcare Ultrospec 2100 Pro UV–Vis-NIR spectrophotometer. Fluorescence spectra were recorded using a Tecan Infinite 200PRO microwell plate reader (Tecan Trading AG, Männedorf, Switzerland). Details on the calculations and the resulting QY values are provided in SI (Figure S3, Table S1).

2.4 2PA cross-section

To experimentally determine the 2PA cross-section of the NPs, the method described by Albota et al. [34] was followed, calibrating with respect to fluorescein (aqueous, 0.1 mM, pH 12, 16 GM). A colloidal NP suspension was excited with vertically polarized excitation light originating from a femtosecond pulsed laser (Insight DS+, Spectra-Physics) tuned at 900 nm, with an output power of 1.85 W and repetition rate of 120 fs. The power incident on the sample was tuned using an achromatic half-wave plate. Under an angle of 90°, fluorescence emission was collected and processed by a Bruker IS/SM 500 spectrometer in combination with an Andor Solis EMCCD camera (iXon Ultra 897). The obtained 2PA cross-sections of the PSMA-encapsulated NPs are listed in SI (Figure S4).

2.5 Electrode fabrication

Gold IDEs were fabricated on borosilicate glass chips by optical lithography as reported previously [22]. Briefly, 4-inch borofloat glass wafers of 0.7 mm thickness were piranha cleaned (1:3 v/v H_2O_2 [30%] H_2SO_4 [98%]) for 20 min. Subsequently, HMDS was spin-coated as an adhesion promoter, followed by Microposit S1818 G2 positive resist (3000 rpm, 30 s) and a 2 min soft bake. Using an EVG 620 illuminator, the resist was patterned and developed for 2 min 30 s in a 1:4 aqueous dilution of Microposit 351 developer. The silicon photomask (soda-lime, inverted) was ordered commercially from Compugraphics (Glenrothes, Scotland). Finally, using a Baltzer BAE370 sputter coater, first a titanium adhesion layer was sputtered for 15 s at 200 W RF-power followed by gold at 50 W for 3 min 20 s. Lift-off was carried out overnight in NMP. The resulting structures have a thickness of roughly 150–200 nm as found by atomic force microscopy (AFM) probing (Figure S5).

Wafers were diced in 1 × 1 cm square chips and mounted and bonded on a printed circuit board (PCB). The PCB has a standard thickness of 1.58 mm and features a square 0.7 mm deep cavity in the center for fitting the glass IDE chip. A center hole of 0.8 mm diameter allows for transmission fluorescence microscopy in addition to reflection microscopy. The top surface of the PCB features five copper bond pads on each side of the glass chip to allow for the individual control of up to five IDE arrays. Using a custom microscope adaptor, the PCB can be mounted upright or upside-down on a microscope stage.

2.6 Sample preparation

After bonding the glass IDE chip to the PCB, the top surface was coated by drying 10 µL of an 0.3 mg/mL collagen fiber solution. The collagen was pregelled for 24 h at 37 °C in a Binder incubator and horn sonicated for 10 s at 1 W (Branson sonifier 150). After drying and rinsing, the fibers were functionalized by incubating 20 µL of 200 nM NP solution for 4 h. The NPs were 30 min beforehand activated through the addition of 5 mM 1-ethyl-3-(3-dimethylaminopropyl)-carbodiimide (EDC) and 5 mM sulfo-*N*-hydroxysulfosuccinimide (s-NHS) to ensure covalent binding to the collagen fibers.

2.7 Fluorescence imaging

1P excited fluorescence imaging was performed on an Olympus IX81 inverted microscope equipped with an X-cite lamp with a maximum output power of 100 W. The excitation light was passed through a 460–495 nm bandpass filter and focused using a 20× objective (Olympus LUCPLFLN20XRC NA 0.45). The average power in the focal plane amounted to ~10 mW. Epi-fluorescence emission was passed through a 510 nm long-pass filter (510IF) and collected using a Hamamatsu Orca-Flash4.0 V2 sCMOS camera.

2PF imaging was performed on an upright Olympus BX61 W1 microscope. The microscope was coupled to a tunable mode-locked femtosecond laser (Insight DS, Spectra Physics) with a repetition rate

of 80 MHz and pulse widths of 120 fs. The laser power in the focal plane was set to 5–20 mW by combining a polarizer and achromatic half-wave plate. The excitation light was focused using a 40× objective (Nikon, 0.80 NA, 3.5 mm WD). Epi-fluorescence emission was passed through a 475 nm long-pass filter and collected using Olympus FV10MP photomultiplier tubes.

Using a custom-made microscope adapter, PCBs were mounted upright on the inverted microscope for 1P excited fluorescence and upside-down on the upright microscope for 2P excited fluorescence imaging. The PCBs were connected to an in-house fabricated high voltage unit supplying DC (direct current) voltages up to 200 V or an amplified function generator (AFG 302 Tektronix function generator and an FLC electronics 20× F20A Voltage amplifier) to generate AC-modulated voltages up to 75 V. For an electrode spacing of 3 µm the corresponding electric field strengths were 600 and 250 kV/cm, respectively. These field strengths are the relevant regime for cellular transmembrane E-fields (in the order of 100 kV/cm).

3 Results and discussion

All three NP types were water-transferred by encapsulation of the native hydrophobic ligands with amphiphilic PSMA. Additionally, QD6 was transferred by exchanging the native ligands for MSA, and QD9 was encapsulated with a silica shell which also results in a direct interaction between the silica matrix and the QD surface, involving most likely an exchange of the native ligands [30]. Details on the experimental protocols can be found in the Materials and Methods section and SI. 1P and 2P excited fluorescence emission spectra of the water-transferred NPs are supplied in SI (Figures S2–S4). The 1P QY were determined relative to rhodamine 6G and amount to (25 ± 2), (42 ± 6) and (69 ± 5)% for QD6-PSMA, QD9-PSMA and QR35-PSMA, respectively (at pH 7.5, 25 °C). Typically, water-transfer greatly reduces the 1P QY due to the interaction of the NP surface with water molecules and oxygen. Compared to state-of-the-art phase transfer protocols, the employed polymer encapsulation protocol guarantees high QY retention in combination with a small hydrodynamic size and excellent long-term stability [26].

The 2PA cross-sections of QD6-PSMA, QD9-PSMA and QR35-PSMA, determined by comparing the 2P emission spectrum with that of fluorescein, were $(24 \pm 4) \times 10^2$ GM, $(7 \pm 1) \times 10^3$ GM and $(22 \pm 4) \times 10^4$ GM, respectively. Details on the experimental determination of the quantum efficiencies and 2PA cross-sections can be found in SI (Figure S4).

To measure the electric field sensitivity of the 1PF and 2PF, NP-decorated collagen fibers were deposited on arrays of gold IDEs – lithographically patterned on glass substrates – with spacings of 3 and 5 µm (see Figure 1A). QD-functionalized collagen may act as an extracellular matrix supporting cell viability in the context of bio-imaging cellular electric fields [22]. For each IDE, the electrode separation was carefully determined using AFM to account for variations in the electric field applied between IDEs. Moreover, QD coated fibers located in the gap do not protrude above the height of the gold structures (SI Figure S5). A typical sample is shown in Figure 1.

3.1 Steady-state E-field dependence of single- and two-photon fluorescence

To determine the steady-state dependence of fluorescence over E-field, an E-field, increased stepwise between 50 and 600 kV/cm, was applied. The fluorescence of the nanoparticles was recorded for 4 s with the electric field switched ON. Upon removal of the external E-field, the particles were left to equilibrate for 60 s before applying the next voltage step. After background subtraction, the electric field sensitivity was calculated as $\Delta F/F_{OFF} \times 100\%$ where $\Delta F = F_{OFF} - F_{ON}$, with F_{ON} and F_{OFF} representing the average fluorescence emission signals over an IDE while the external electric field was turned ON and OFF, respectively.

In Figure 2, the percentual fluorescence decrease ($\Delta F/F_{OFF}$) is shown as a function of external E-field. The data are grouped per particle, panels *a*, *b* and *c* showing the 1PF and 2PF E-field sensitivities of QD6-PSMA, QD9-PSMA and QR35-PSMA particles, respectively. For each NP type the data were acquired over several 3 and 5 µm spaced IDEs on four distinct PCBs, with at least two IDEs per chip. Graphs showing the experimental data grouped by excitation mechanism (1P vs. 2P) are provided in SI (Figure S6). The effect of different 2P excitation wavelengths on the observed E-field sensitivities was investigated in experiments at an excitation wavelength of 950 and 1000 nm and has no impact on the results (Figure S7).

The effect of a strong electric field on the QDs fluorescence (1PF and 2PF) is known to be a combination of the QCSE and QD ionization [10, 35–37]. In the QCSE effect, the reduced overlap of the electron and hole wave functions causes a reduction of the radiative decay rate. This results in a decrease of the fluorescence that depends quadratically on the applied electric field. In the case of QD ionization, one of the photo-excited carriers, either electron or hole, is ejected from the quantum dot (either thermally or via tunneling) and localized at the QD surface [5]. Photo-excitation of ionized QDs results in a strong quenching of fluorescence, a phenomenon that is known at the single particle level as fluorescence intermittency or "blinking" [38–40]. Nevertheless, the electric field decreases the

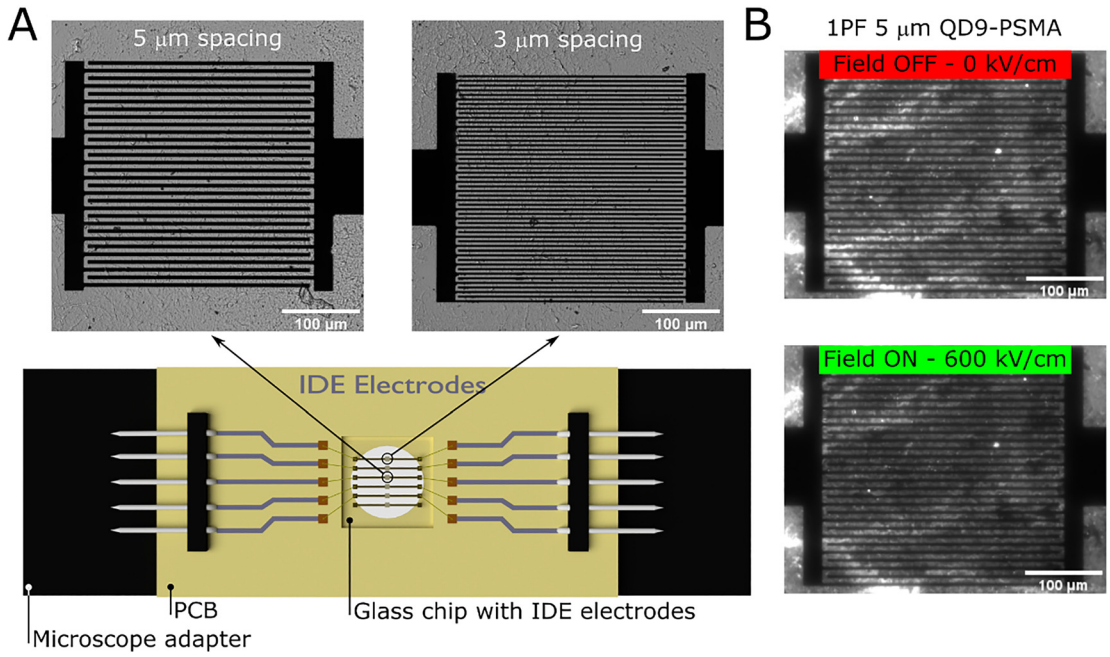

Figure 1: A. Illustration of a PCB with a central glass chip containing an array of IDEs with 5 or 3 µm separation. The bright field microscopy images show both of these electrodes coated with collagen/QD9-PSMA; B. 1PF image of the quasi-type-II QD9-PSMA on a 5 µm spaced IDE with the E-field switched OFF or ON (600 kV/cm).

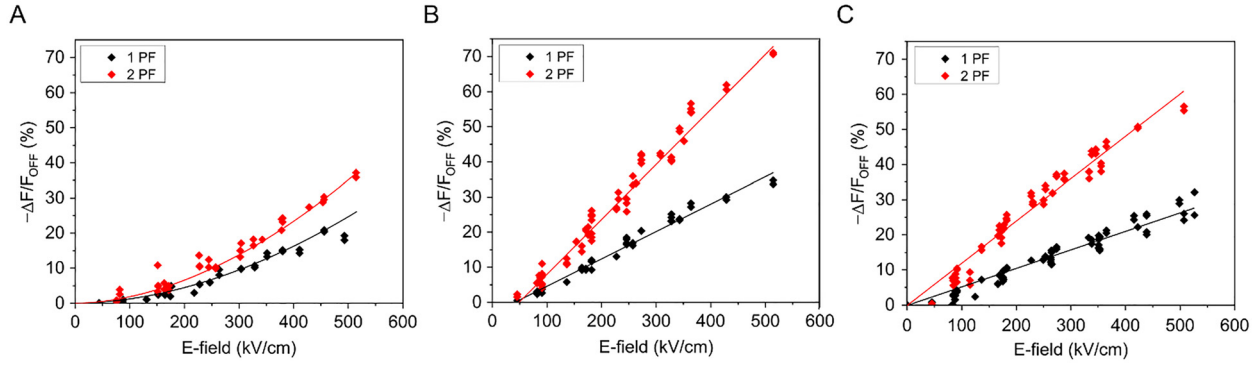

Figure 2: Electric field induced decrease of the fluorescence intensity, $\Delta F/F_{OFF}$, under 1P excitation (460–495 nm) in black and 2P excitation (900 nm) in red for the type-I QD6-PSMA (panel A), the quasi-type-II QD9-PSMA (panel B) and the quasi-type-II QR35-PSMA (panel C). Every point represents a single measurement. Data are fit with a power low $y_0 + a.x^b$. The obtained values for y_0, a and b are listed in Table 2.

Table 2: Fit parameters of the power laws performed on the data presented in Figure 2, panels a through c.

	1PF			2PF		
NP	y_0	a	b	y_0	a	b
QD6-PSMA	0	$(9.3 \pm 0.3) \times 10^{-5}$	2	0	$(1.50 \pm 0.04) \times 10^{-4}$	2
QD9-PSMA	(-3.2 ± 0.5)	$(7.8 \pm 0.2) \times 10^{-2}$	1	(-8 ± 2)	$(1.57 \pm 0.05) \times 10^{-1}$	1
QR35-PSMA	0	$(5.3 \pm 0.1) \times 10^{-2}$	1	0	$(1.20 \pm 0.02) \times 10^{-1}$	1

confinement barriers for electrons and holes and thereby increases the probability for ionization. As the number of ionized QDs in an ensemble of QDs increases with increasing field strength, the population of quenched QDs increases, resulting in a decrease of the ensemble fluorescence. After some time, the ejected carrier returns to the QD, neutrality is restored together with the original fluorescence. Experimental studies showed this to occur at time scales of seconds to tens of seconds [41]. QD ionization has been identified as the main contribution to the fluorescence decrease in an externally applied electric field [9].

Previously, it has been shown experimentally on single CdSe and core–shell QDs that the contribution of the QCSE to the decrease in fluorescence intensity is proportional to the square of the electric field for field strengths up to 250 kV/cm [10, 42]. Here, we find a quadratic dependence of $\Delta F/F_{OFF}$ on the external E-field (see Table 2), irrespective of the mode of excitation. For the quasi-type-II QD9-PSMA, on the other hand, a quadratic curve doesn't fit the experimental data well. For field strengths larger than 150 kV/cm, Figure 2B displays a linear behavior. This likely indicates a more dominant contribution of QD ionization to the fluorescence quenching at high field strengths [5]. For QR35-PSMA, finally, we found a linear dependence for both 1P excitation and 2P excitation, similar to previous literature reports [5, 10]. Due to the anisotropic shape of the rods, the exciton has a net dipole and the QCSE is linear in the external electric field. For an ensemble of nonoriented rods, the QCSE could hence result in an increase or decrease of the PL of a specific NP. This indicates that the major contribution to the observed intensity change in Figure 2C is again NP ionization. NP orientation along the direction of the E-field would potentially enhance the quenching even more.

The E-field sensitivity for each type of particle was consistently larger under 2P excitation compared to 1P excitation. For an E-field of 300 kV/cm, the 1P quantum efficiency of the NPs was reduced by (10 ± 1), (20 ± 2) and (16 ± 2)% respectively for QD6-PSMA, QD9-PSMA and QR35-PSMA. Based on the fit in Figure 2, the E-field sensitivity of the fluorescence intensity of QD6-PSMA was a factor (1.61 ± 0.04) increased under 2P excitation with respect to 1P excitation. For the quasi-type-II NPs an enhancement by (1.9 ± 0.2) and (2.5 ± 0.2) was found for QD9-PSMA and QR35-PSMA, respectively. The mechanism behind the enhanced E-field sensitivity is unclear. It is possible that the boosted fluorescence decrease under 2P excitation is due to E-field sensitivity of the 2PA cross-section as was previously hypothesized to be the case for temperature [21]. The enhancement of the E-field sensitivity scaled with the magnitude of the 2PA cross-section, being largest for QR35-PSMA ((22 ± 4) × 10^4 GM), followed by QD9-PSMA ((7 ± 1) × 10^3 GM) and finally QD6-PSMA ((24 ± 4) × 10^2 GM). The large 2PA cross-sections of semiconductor nanostructures are commonly attributed to Lorentz local field effect [2, 37, 43], supporting the hypothesis that external E-fields will impact the 2PA cross-section as well. Alternatively, considering that QD ionization provides a dominant contribution to the fluorescence quenching, intraband processes of 2P excited charge carriers can further increase nonradiative decay rates [44, 45]. Single particle spectroscopy experiments are needed to further elucidate the exact mechanism(s) at play.

Next, we briefly studied to what extent the level of ionization can be controlled through the choice of the QD coating material. For this purpose, we measured the electric field dependence of silica-coated QD9 (QD9-SiO_2) and mercaptosuccinic acid coated QD6 (QD6-MSA) particles under 1P excitation. It is known that the type of ligand (electron-donating, etc.) affects the level of QD ionization through passivation of existing surface traps [46]. Figure 3A shows the relative change in fluorescence intensity of QD9-PSMA (black) and QD9-SiO_2 (red). The change in intensity of the silica-coated particles was much lower compared to the PSMA-encapsulated particles. Similarly, the electric field sensitivity of QD6-MSA was much stronger with respect to the PSMA-encapsulated variant and displayed saturation behavior at high field strengths that was not observed in any of the PSMA-encapsulated NPs. This suggests that the main contribution to the E-field sensitivity is indeed QD surface ionization causing here a deviation from the quadratic trend.

Thus, the ligand coating of the nanoparticle has a large effect on the ionization and hence the electric field sensitivity. For QD9-PSMA at 300 kV/cm, the sensitivity was (24 ± 2)% while for the same particles with SiO_2 surface passivation it was only (5.4 ± 0.5)% (roughly a fivefold decrease). For QD6, the MSA-coating resulted in a fivefold increase.

3.2 AC E-field fluorescence modulation

We next studied the temporal behavior of the fluorescence of QD6-PSMA, QD9-PSMA and QR35-PSMA with an applied E-field of (300 ± 5) kV/cm. Again, the E-field was switched on for 4 s and the 1PF was continuously recorded until the fluorescence emission recovered to its original intensity (Figure 4).

For QD6-PSMA and QD9-PSMA, switching the field ON did not instantly lower the QD's fluorescence to its

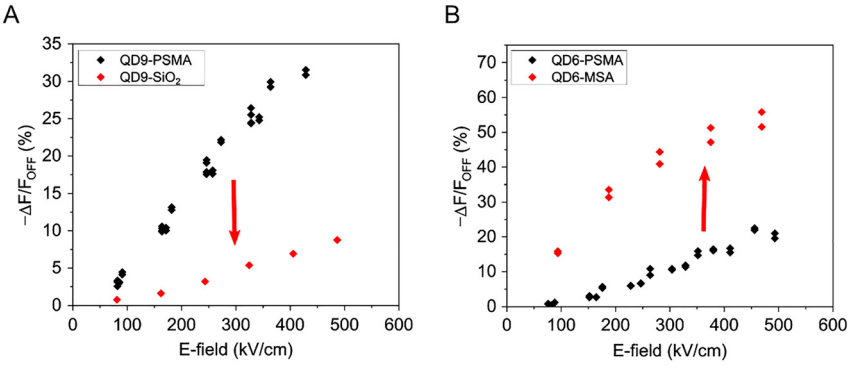

Figure 3: $\Delta F/F_{OFF}$ as a function of electric field under 1P excitation (460–495 nm) for (A) the quasi-type-II QD9-PSMA (black) and QD9-SiO_2 (red) and for (B) the type-I QD6-PSMA (black) and QD6-MSA (red).

minimum level but a clear ON transient was observed. This ON transient was significantly faster for QD9-PSMA than for QD6-PSMA. Similarly, upon switching the external E-field off, an OFF transient was recorded for both NPs. For QR35-PSMA, on the other hand, switching the field ON immediately lowered the fluorescence to a minimum followed by a small recovery phase, i.e. a brightening. We hypothesize that when the E-field is turned on the energy barriers for surface trap states are reduced and electrons are trapped in the surface states. A 'field-induced' passivation of the trap states in QRs then causes an increase in the radiative decay rate. For the quasi-type-II QD, QD9-PSMA, a small amount of photo-brightening could only be observed for very large E-fields strengths (>400 kV/cm) (see Figure 4D). This different behavior between QR and QD can be explained by the larger surface area of the QRs in combination with different native ligands (oleic acid for QD9 vs. phosphonic acids for QR35). Photo-brightening

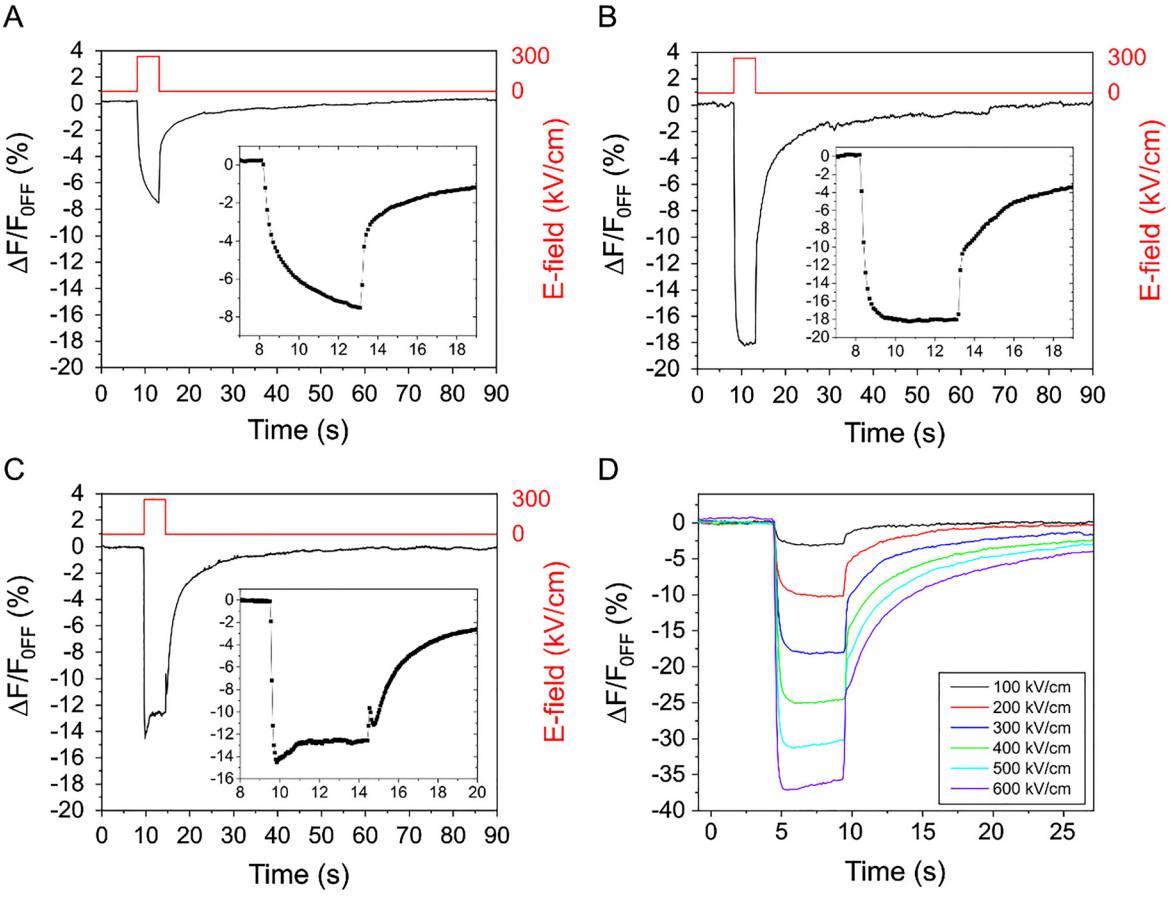

Figure 4: Temporal behavior of the 1P excitation $\Delta F/F_{OFF}$ for an applied field of (300 ± 5) kV/cm for (A) the type-I QD6-PSMA, (B) the quasi-type-II QD9-PSMA and (C) the quasi-type-II QR35-PSMA; (D) $\Delta F/F_{OFF}$ transients of the quasi-type-II QD9-PSMA for a range of electric field strengths.

was not observed for QD6-PSMA, as could be expected for type-I NPs, the outer surface of which is effectively shielded by a ZnS layer.

Upon switching the E-field OFF, again a slow fluorescence recovery is recorded, with characteristic time scales in the seconds to tens of seconds range. The observed recovery time (see Figure 4D) can be linked to field-induced defect creation and hence was more prominent in larger particles and (quasi-)type-II particles. This transient behavior is intrinsic to carrier trapping as it is not observed for spectral shifts in response to externally applied E-fields, which occur instantaneously [7, 10]. The capacitance of the IDE was in the pF range and can therefore not underlie the observed delay in the fluorescence recovery [47, 48].

For transmembrane voltage imaging in living cells, the NPs are required to respond to fast switching electrical fields with magnitudes up to 150 kV/cm. For cardiomyocytes, the typical duration of an action potential is around 200–300 ms, with physiologically relevant beat frequencies ranging from 0.2 to 3 Hz. Neurons, on the other hand, fire much faster, up to kHz rates in the case of cortical neurons. Hence, the slow ON and OFF QD fluorescence transients will clearly limit the E-field sensitivity in cellular preparations.

To experimentally probe the responses to field transients, alternating voltages were applied to the IDEs. Figures 5 and 6 show the corresponding traces of QD9-PSMA and QR35-PSMA under 1P and 2P illumination for a square stimulation wave with a high level of 150 kV/cm, a low level of 0 kV/cm and a 50% duty cycle. The applied frequencies are 0.5, 1, 2, 5 and 10 Hz with a frame sampling rate of 200 Hz (1P) and line scanning frequency of 100 Hz (2P). In order to achieve the required temporal resolution in 2P imaging, a single line of approximately 200 pixels is imaged. This causes the signal-to-noise ratio (SNR) in the 2PF traces to be drastically reduced compared to the 1PF traces. Nevertheless, the fluorescence traces clearly illustrate that a frequency increase suppressed the slow fluorescence recovery and hence decreased $\Delta F/F_{OFF}$. Similar behavior was observed for QD6-PSMA (Figure S8). The E-field sensitivity $\Delta F/F_{OFF}$ as a function of AC frequency is summarized in Figure 7. From 5 Hz onwards the 1P sensitivity stabilizes at (1.8 ± 0.6), (5.8 ± 0.2) and (3.4 ± 0.4)% for QD6-PSMA, QD9-PSMA and QR35-PSMA respectively. For 2P, the fluorescence changes are (2.4 ± 0.6), (10.1 ± 0.8) and (7.9 ± 0.5)% for QD6-PSMA, QD9-PSMA and QR35-PSMA. From frequencies above 2 Hz, QD9-PSMAs outperform QR35-PSMAs as the latter have much slower OFF-transients. This behavior is particularly relevant for biological applications as this OFF transient defines the reliable detection limit in excitable cells where the transmembrane E-field decreases only for short periods

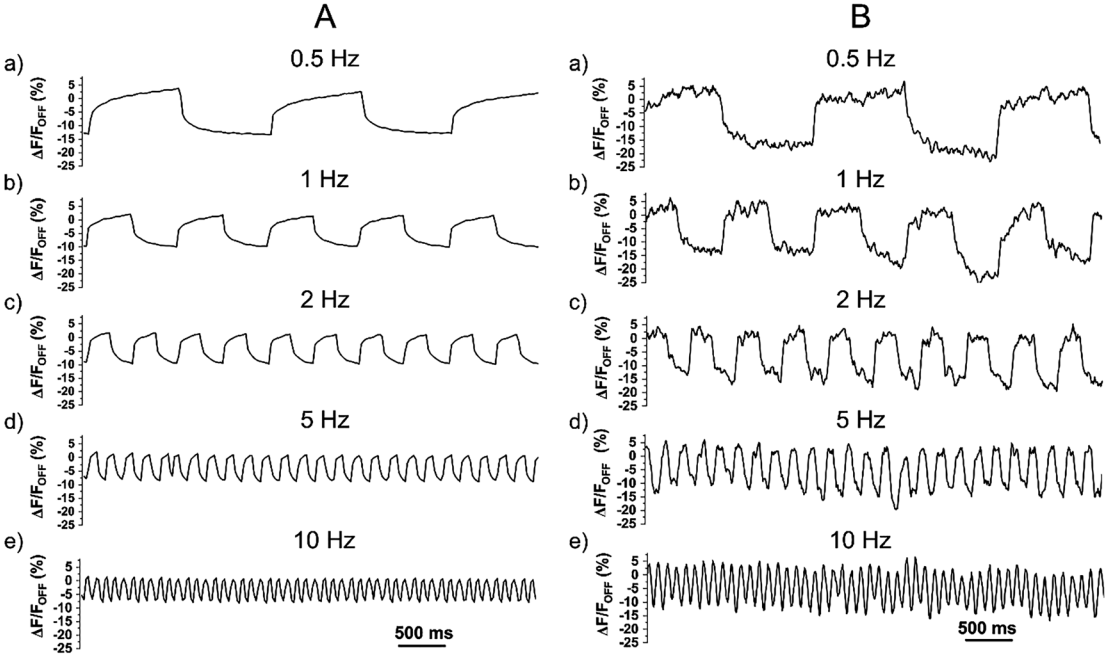

Figure 5: Effect of a frequency modulated E-field with an amplitude of 150 kV/cm on the fluorescence changes of the quasi-type-II QD9-PSMA under (A) 1P excitation (460–495 nm) and (B) 2P excitation (900 nm) for different frequencies.

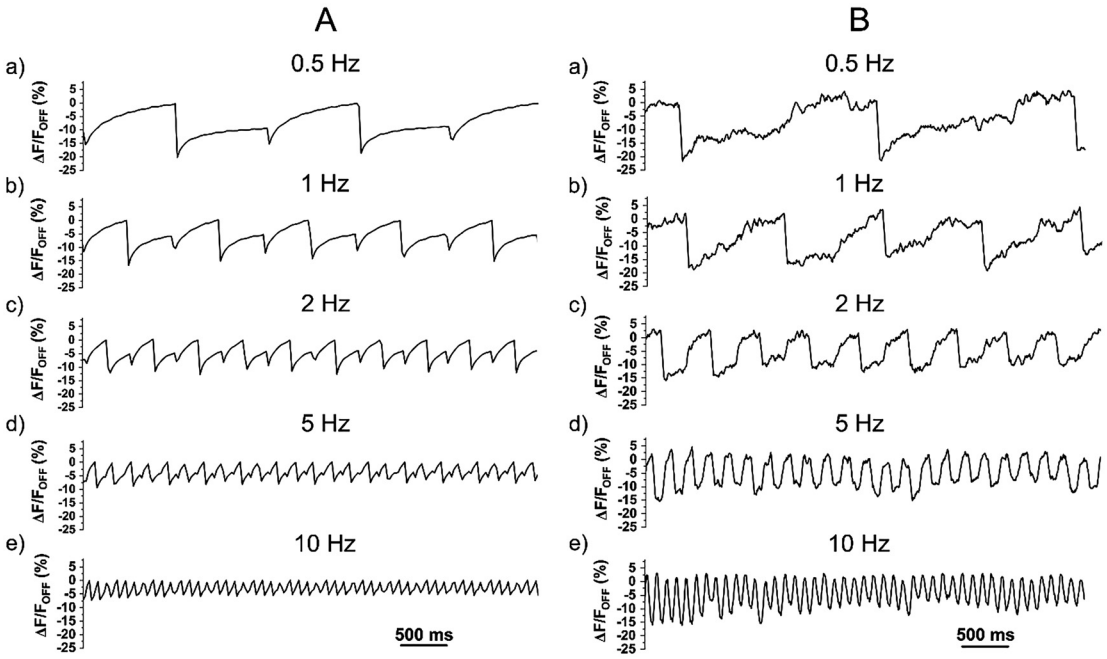

Figure 6: Effect of a frequency modulated E-field with an amplitude of 150 kV/cm on the fluorescence changes of QR35-PSMA under (A) 1P excitation (460–495 nm) and (B) 2P excitation (900 nm).

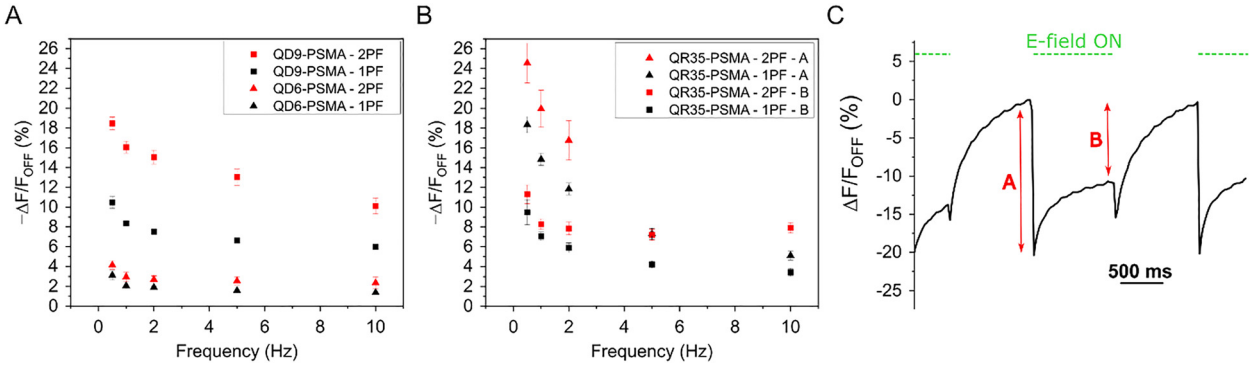

Figure 7: (A) $\Delta F/F_{OFF}$ as a function of the frequency of the applied electric field for the type-I QD6-PSMA and the quasi-type-II QD9-PSMA under 1P excitation (460–495 nm, black) and 2P excitation (900 nm, red). (B) $\Delta F/F_{OFF}$ as a function of the frequency for the quasi-type-II QR35-PSMA at both locations indicated in the 0.5 Hz–150 kV/cm modulated fluorescence trace shown in panel C.

between successive APs. Nevertheless, changes in 2PF are consistently larger compared to 1PF for all three NPs (see Figure 7).

3.3 Simulated cardiac action potential

The result of an experiment, simulating a 60 bpm train of cardiac action potentials is shown in Figure 8. APs were simulated by a square wave with a low level of –150 kV/cm, corresponding to the resting membrane potential, a high level of 0 kV/cm and 15% duty cycle. The percentual change was calculated as $\Delta F/F_{ON}$ using the NP fluorescence intensity at –150 kV/cm as baseline.

Compared to a 3.3 Hz AC voltage wave, which corresponds to an OFF-level duration of 300 ms, NPs are much longer under the bias of the –150 kV/cm E-field (the resting potential) using the 60 bpm protocol. For QD6-PSMA and QD9-PSMA the fluorescence intensity is stable (over long periods of time and several repetitions) and the fluorescence signals follow the transient fields with the expected sensitivities. In line-scanning mode (200 pixels, 100 Hz), which is necessary to achieve the required temporal resolution, the SNR is drastically decreased (noise levels up to

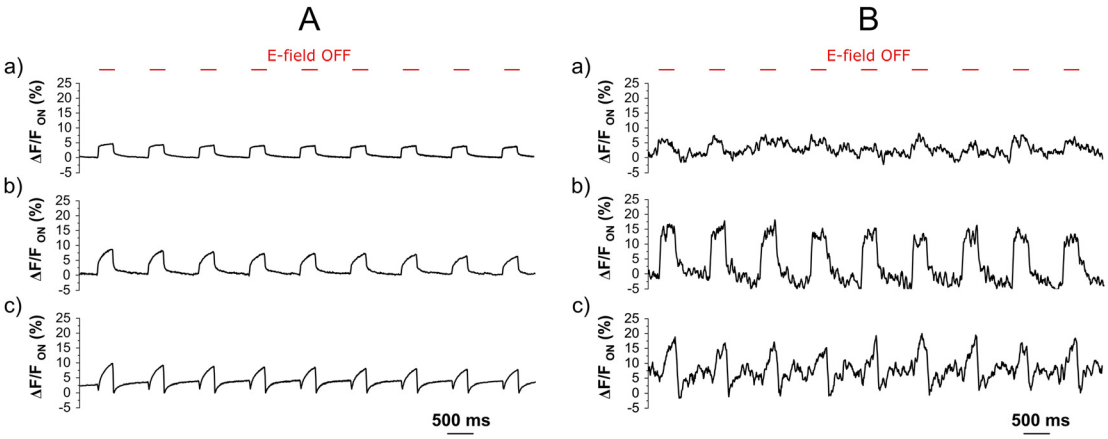

Figure 8: Optical response to a simplified 60 bpm cardiac action potential train with a resting potential corresponding to an electric field of –150 kV/cm and a transient amplitude of the same magnitude of (a) the type-I QD6-PSMA, (b) the quasi-type-II QD9-PSMA and (c) the quasi-type-II QR35-PSMA under 1P excitation (460–495 nm, panel A) and 2P excitation (900 nm, panel B).

3%), rendering the QD6-PSMA 2PF signal too low to detect the E-field transients. The 2PF signal of QD9-PSMA, on the other hand, exhibits the highest SNR in response to transient fields. For the QR35-PSMA the observed photobrightening under E-field switching dominates the response such that the fluorescence changes do not follow the E-field profiles well. This is in striking contrast to the 2PF responses to AC modulated fields presented in Figures 5 and 6. The change in duty cycle (i.e. from 50% in Figures 5–7 to 15% in Figure 8) clearly favors photobrightening when the E-field is switched ON at the expense of the (slower) 2PF recovery when the E-field is briefly switched OFF.

4 Conclusion and perspectives

Previous studies on the E-field sensitivity of the fluorescence intensity of type-I and (quasi-)type-II semiconductor NPs mainly report 1P data, obtained at various field strengths and often compare sensitivities at E-fields as large as 400 kV/cm. When imaging cell transmembrane voltages, however, the local E-fields may vary from steady-state to kHz modulated signals and also various combinations of NP types and coatings may be used. Moreover, despite the hypothesized potential and significant research efforts, attempts to incorporate these NPs within cellular membranes and use them for direct monitoring of the electric activity by 1PF have resulted in measured fluorescence changes below expectations.

In this study, we show that the E-field sensitivity is greatly enhanced under 2P excitation compared to 1P excitation. We have characterized in detail the E-field response of the fluorescence of PSMA-encapsulated NPs with three different configurations. By carefully controlling the NP shell, we show that the surface coating has an important role in the E-field sensitivity by controlling the extent to which QD ionization contributes to the fluorescence quenching.

Additionally, we observe a slow E-field OFF recovery time, in the order of seconds, that causes a significant reduction in the sensitivity to AC modulated E-fields from frequencies as low as 1 Hz. This slow recovery time constitutes a major limitation on the applicability of these NPs for the detection of fast neuronal signals, where action potentials have a duration of approximately 2 ms. For monitoring cardiomyocyte activity, on the other hand, the impact is rather limited as demonstrated by calibration experiments using a simplified model for a 60 bpm cardiac action potential train. These results demonstrate that electrical activity with temporal patterns in this range can be clearly detected. In this experiment, the QD9-PSMA particles are found to perform best with an AP detection sensitivity of about (8 ± 1)% under 1P excitation and about double (i.e. (14 ± 3)%) under 2P excitation.

It is important to note, however, that the quasi-type-II QRs were not aligned along the direction of the electrical field. Alignment is expected to increase the response significantly and could be attempted to further increase the sensitivity. Large 2PF changes in response to applied fields indicate that high QY, nonsymmetric structures such as QRs, might have superior performance as compared to other probe types for imaging cell activity with multiphoton methods given that oriented membrane insertion can be achieved.

All NPs are particularly suitable for imaging biological samples by multiphoton methods due to the inherently higher spatial and temporal resolution of multiphoton microscopy combined with lower scattering and absorption at longer wavelengths. The SNR of the 2PF response of a single line scan, though significantly lower than in the presented 1PF traces, is found to be satisfactory for detecting QY changes under the influence of a fast switching E-field. It strengthens our belief that 2PF imaging could improve future attempts to measure QY changes of cell membrane inserted NPs, despite the limited collection of potentially E-field responsive pixels.

Abbreviations

1P(F)/2P(F)	single-photon (fluorescence)/two-photon (fluorescence)
2PA	two-photon absorption cross-section
3D	three dimensional
AC	alternating current
AP	action potential
AFM	atomic force microscopy
bpm	beats per minute
DC	direct current
EDC	1-ethyl-3-(3-dimethylaminopropyl)-carbodiimide
E-field	electric field
ethNH$_2$	ethanolamine
GEVI	genetically encoded voltage indicator
GM	Goeppert–Mayer
HMDS	hexamethyldisilazane
HEK	human embryonic kidney
HEPES	4-(2-hydroxyethyl)-1-piperazineethanesulfonic acid
HPA	hexylphosphonic acid
IDE	interdigitated electrode
M600	jeffamine polyetheramine M-600
MeOH	methanol
MSA	mercaptosuccinic acid
NMP	1-methyl-2-pyrrolidone
NP	nanoparticle
OA	oleic acid
ODE	1-octadecene
ODPA	octadecylphosphonic acid
PCB	printed circuit board
PEG	polyethylene glycol
PPG	polypropylene glycol
PSMA	poly-styrene-*co*-maleic anhydride
PVP	polyvinylpyrrolidone
QCSE	quantum-confined Stark effect
QD/QR	quantum dot/quantum rod
QY	quantum yield
RF	radio frequency
rpm	rounds per minute
sCMOS	scientific Complementary metal-oxide-semiconductor
s-NHS	sulfo-*N*-hydroxysulfosuccinimide
SNR	signal-to-noise ratio
TEM	transmission electron microscopy
TMAH	tetramethylammonium hydroxide pentahydrate
TOP(O)	tri-*n*-octyl phosphine (oxide)

Author contributions: All the authors have accepted responsibility for the entire content of this submitted manuscript and approved submission.
Research funding: S. Jooken acknowledges the financial support by the Flanders Research Foundation (FWO) – strategic basic research doctoral grant 1SC3819N. C. Bartic, G. Callewaert and O. Deschaume acknowledge the financial support by the Flanders Research Foundation (FWO grant G0947.17N) and KU Leuven research grants OT/14/084 and C14/18/061. T. Verbiest acknowledges financial support from the Hercules Foundation, grant AKUL/11/15.
Conflict of interest statement: The authors declare no conflicts of interest regarding this article.

References

[1] G. Nagamine, J. O. Rocha, L. G. Bonato, et al., "Two-photon absorption and two-photon-induced gain in Perovskite quantum dots," *J. Phys. Chem. Lett.*, vol. 9, pp. 3478–3484, 2018.
[2] R. Scott, A. W. Achtstein, A. Prudnikau, et al., "Two photon absorption in II–VI semiconductors: the influence of dimensionality and size," *Nano Lett.*, vol. 15, pp. 4985–4992, 2015.
[3] F. Pinaud, S. Clarke, A. Sittner, and M. Dahan, "Probing cellular events, one quantum dot at a time," *Nat. Methods*, vol. 7, pp. 275–285, 2010.
[4] Y. R. Kumar, K. Deshmukh, K. K. Sadasivuni, and S. K. K. Pasha, "Graphene quantum dot based materials for sensing, bio-imaging and energy storage applications: a review," *RSC Adv.*, vol. 10, pp. 23861–23898, 2020.
[5] C. E. Rowland, K. Susumu, M. H. Stewart, et al., "Electric field modulation of semiconductor quantum dot photoluminescence: insights into the design of robust voltage-sensitive cellular imaging probes," *Nano Lett.*, vol. 15, pp. 6848–6854, 2015.
[6] S. I. Pokutnyi, L. Jacak, J. Misiewicz, W. Salejda, and G. G. Zegrya, "Stark effect in semiconductor quantum dots," *J. Appl. Phys.*, vol. 96, pp. 1115–1119, 2004.
[7] O. Bar-Elli, D. Steinitz, G. Yang, et al., "Rapid voltage sensing with single nanorods via the quantum confined stark effect," *ACS Photonics*, vol. 5, pp. 2860–2867, 2018.
[8] M. Caglar, R. Pandya, J. Xiao, et al., "All-optical detection of neuronal membrane depolarization in live cells using colloidal quantum dots," *Nano Lett.*, vol. 19, pp. 8539–8549, 2019.
[9] A. L. Efros, J. B. Delehanty, A. L. Huston, I. L. Medintz, M. Barbic, and T. D. Harris, "Evaluating the potential of using quantum dots for monitoring electrical signals in neurons," *Nat. Nanotechnol.*, vol. 13, pp. 278–288, 2018.
[10] K. Park, Z. Deutsch, J. J. Li, D. Oron, and S. Weiss, "Single molecule quantum-confined stark effect measurements of semiconductor nanoparticles at room temperature," *ACS Nano*, vol. 6, pp. 10013–10023, 2012.
[11] Y. Kuo, J. Li, X. Michalet, et al., "Characterizing the quantum-confined stark effect in semiconductor quantum dots and

nanorods for single-molecule electrophysiology," *ACS Photonics*, vol. 5, pp. 4788–4800, 2018.
[12] E. Rothenberg, M. Kazes, E. Shaviv, and U. Banin, "Electric field induced switching of the fluorescence of single semiconductor quantum rods," *Nano Lett.*, vol. 5, pp. 1581–1586, 2005.
[13] N. N. Hewa-Kasakarage, M. Kirsanova, A. Nemchinov, et al., "Radiative recombination of spatially extended excitons in (ZnSe/CdS)/CdS heterostructured nanorods," *J. Am. Chem. Soc.*, vol. 131, pp. 1328–1334, 2009.
[14] S. A. Empedocles and M. G. Bawendi, "Quantum-confined stark effect in single CdSe nanocrystallite quantum dots," *Science (80-)*, vol. 278, pp. 2114–2117, 1997.
[15] O. K. Nag, M. E. Muroski, D. A. Hastman, et al., "Nanoparticle-mediated visualization and control of cellular membrane potential: strategies, progress, and remaining issues," *ACS Nano*, vol. 14, pp. 2659–2677, 2020.
[16] O. K. Nag, M. H. Stewart, J. R. Deschamps, et al., "Quantum dot–peptide–fullerene bioconjugates for visualization of in vitro and in vivo cellular membrane potential," *ACS Nano*, vol. 11, pp. 5598–5613, 2017.
[17] G. Chen, Y. Zhang, Z. Peng, D. Huang, C. Li, and Q. Wang, "Glutathione-capped quantum dots for plasma membrane labeling and membrane potential imaging," *Nano Res.*, vol. 12, pp. 1321–1326, 2019.
[18] K. Park, Y. Kuo, V. Shvadchak, et al., "Membrane insertion of—and membrane potential sensing by—semiconductor voltage nanosensors: feasibility demonstration," *Sci. Adv.*, vol. 4, p. e1601453, 2018.
[19] J. Park, Y. Kuo, J. Li, Y.-L. Huang, E. W. Miller, and S. Weiss, "Improved surface functionalization and characterization of membrane-targeted semiconductor voltage nanosensors," *J. Phys. Chem. Lett.*, vol. 10, pp. 3906–3913, 2019.
[20] A. Ludwig, P. Serna, L. Morgenstein, et al., "Development of lipid-coated semiconductor nanosensors for recording of membrane potential in neurons," *ACS Photonics*, vol. 7, pp. 1141–1152, 2020.
[21] L. M. Maestro, E. M. Rodríguez, F. S. Rodríguez, et al., "CdSe quantum dots for two-photon fluorescence thermal imaging," *Nano Lett.*, vol. 10, pp. 5109–5115, 2010.
[22] S. Jooken, Y. De Coene, O. Deschaume, et al., "Quantum dot-functionalized extracellular matrices for in situ monitoring of cardiomyocyte activity," *ACS Appl. Nano Mater.*, vol. 3, pp. 6118–6126, 2020.
[23] M. Cirillo, T. Aubert, R. Gomes, et al., "'Flash' synthesis of CdSe/CdS core–shell quantum dots," *Chem. Mater.*, vol. 26, pp. 1154–1160, 2014.
[24] E. Drijvers, J. De Roo, P. Geiregat, K. Fehér, Z. Hens, and T. Aubert, "Revisited Wurtzite CdSe synthesis: a gateway for the versatile flash synthesis of multishell quantum dots and rods," *Chem. Mater.*, vol. 28, pp. 7311–7323, 2016.
[25] L. Carbone, C. Nobile, M. De Giorgi, et al., "Synthesis and micrometer-scale assembly of colloidal CdSe/CdS nanorods prepared by a seeded growth approach," *Nano Lett.*, vol. 7, pp. 2942–2950, 2007.
[26] E. E. Lees, T.-L. Nguyen, A. H. A. Clayton, and P. Mulvaney, "The preparation of colloidally stable, water-soluble, biocompatible, semiconductor nanocrystals with a small hydrodynamic diameter," *ACS Nano*, vol. 3, pp. 1121–1128, 2009.
[27] B. Pong, B. L. Trout, and J. Lee, "Modified ligand-exchange for efficient solubilization of CdSe/ZnS quantum dots in water: a procedure guided by computational studies," *Langmuir*, vol. 24, pp. 5270–5276, 2008.
[28] S. Parani, G. Bupesh, E. Manikandan, K. Pandian, and O. S. Oluwafemi, "Facile synthesis of mercaptosuccinic acid-capped CdTe/CdS/ZnS core/double shell quantum dots with improved cell viability on different cancer cells and normal cells," *J. Nanoparticle Res.*, vol. 18, p. 347, 2016.
[29] T. Aubert, S. J. Soenen, D. Wassmuth, et al., "Bright and stable CdSe/CdS@SiO_2 nanoparticles suitable for long-term cell labeling," *ACS Appl. Mater. Interfaces*, vol. 6, pp. 11714–11723, 2014.
[30] A. Biermann, T. Aubert, P. Baumeister, E. Drijvers, Z. Hens, and J. Maultzsch, "Interface formation during silica encapsulation of colloidal CdSe/CdS quantum dots observed by in situ Raman spectroscopy," *J. Chem. Phys.*, vol. 146, p. 134708, 2017.
[31] E. Drijvers, J. Liu, A. Harizaj, et al., "Efficient endocytosis of inorganic nanoparticles with zwitterionic surface functionalization," *ACS Appl. Mater. Interfaces*, vol. 11, pp. 38475–38482, 2019.
[32] D. Magde, R. Wong, and P. G. Seybold, "Fluorescence quantum yields and their relation to lifetimes of rhodamine 6G and fluorescein in nine solvents: improved absolute standards for quantum yields," *Photochem. Photobiol.*, vol. 75, pp. 327–334, 2007.
[33] C. Würth, M. Grabolle, J. Pauli, M. Spieles, and U. Resch-Genger, "Relative and absolute determination of fluorescence quantum yields of transparent samples," *Nat. Protoc.*, vol. 8, pp. 1535–1550, 2013.
[34] M. A. Albota, C. Xu, and W. W. Webb, "Two-photon fluorescence excitation cross sections of biomolecular probes from 690 to 960 nm," *Appl. Opt.*, vol. 37, p. 7352, 1998.
[35] G. W. Wen, J. Y. Lin, H. X. Jiang, and Z. Chen, "Quantum-confined Stark effects in semiconductor quantum dots," *Phys. Rev. B*, vol. 52, pp. 5913–5922, 1995.
[36] J. Seufert, M. Obert, M. Scheibner, et al., "Stark effect and polarizability in a single CdSe/ZnSe quantum dot," *Appl. Phys. Lett.*, vol. 79, pp. 1033–1035, 2001.
[37] B. Zhu, F. Wang, C. Liao, et al., "Size confinement and origins of two-photon absorption and refraction in CdSe quantum dots," *Opt. Express*, vol. 27, p. 1777, 2019.
[38] J. J. Peterson and D. J. Nesbitt, "Modified power law behavior in quantum dot blinking: a novel role for biexcitons and auger ionization," *Nano Lett.*, vol. 9, pp. 338–345, 2009.
[39] G. Yuan, D. E. Gómez, N. Kirkwood, K. Boldt, and P. Mulvaney, "Two mechanisms determine quantum dot blinking," *ACS Nano*, vol. 12, pp. 3397–3405, 2018.
[40] A. L. Efros and D. J. Nesbitt, "Origin and control of blinking in quantum dots," *Nat. Nanotechnol.*, vol. 11, pp. 661–671, 2016.
[41] P. Lochner, A. Kurzmann, J. Kerski, et al., "Real-time detection of single auger recombination events in a self-assembled quantum dot," *Nano Lett.*, vol. 20, pp. 1631–1636, 2020.
[42] L. I. Gurinovich, A. A. Lutich, A. P. Stupak, et al., "Luminescence in quantum-confined cadmium selenide nanocrystals and nanorods in external electric fields," *Semiconductors*, vol. 43, pp. 1008–1016, 2009.
[43] X. Hu, Y. Zhang, D. Guzun, et al., "Photoluminescence of InAs/GaAs quantum dots under direct two-photon excitation," *Sci. Rep.*, vol. 10, p. 10930, 2020.
[44] Y. Qu, W. Ji, Y. Zheng, and J. Y. Ying, "Auger recombination and intraband absorption of two-photon-excited carriers in colloidal CdSe quantum dots," *Appl. Phys. Lett.*, 2007, https://doi.org/10.1063/1.2716067.

[45] F. T. Rabouw, R. Vaxenburg, A. A. Bakulin, et al., "Dynamics of intraband and interband auger processes in colloidal core–shell quantum dots," *ACS Nano*, vol. 9, pp. 10366–10367, 2015.
[46] S. J. Lim, L. Ma, A. Schleife, and A. M. Smith, "Quantum dot surface engineering: toward inert fluorophores with compact size and bright, stable emission," *Coord. Chem. Rev.*, vols. 320–321, pp. 216–237, 2016.
[47] G. González, E. Kolosovas-Machuca, E. López-Luna, H. Hernández-Arriaga, and F. González, "Design and fabrication of interdigital nanocapacitors coated with HfO_2," *Sensors*, vol. 15, pp. 1998–2005, 2015.
[48] R. Igreja and C. J. Dias, "Analytical evaluation of the interdigital electrodes capacitance for a multi-layered structure," *Sens. Actuators A Phys.*, vol. 112, pp. 291–301, 2004.

Supplementary Material: The online version of this article offers supplementary material (https://doi.org/10.1515/nanoph-2021-0077).